



# Reply to Comment by Jennings et al. on "Investigating Earth's Formation History Through Copper and Sulfur Metal-Silicate Partitioning During Core-Mantle Differentiation"

B. Mahan, J. Siebert, J. Badro, S. Borensztajn, F. Moynier

## ► To cite this version:

B. Mahan, J. Siebert, J. Badro, S. Borensztajn, F. Moynier. Reply to Comment by Jennings et al. on "Investigating Earth's Formation History Through Copper and Sulfur Metal-Silicate Partitioning During Core-Mantle Differentiation". *Journal of Geophysical Research: Solid Earth*, 2019, 124, pp.12,845-12,853. 10.1029/2019JB017599 . insu-03586588

HAL Id: insu-03586588

<https://insu.hal.science/insu-03586588>

Submitted on 24 Feb 2022

**HAL** is a multi-disciplinary open access archive for the deposit and dissemination of scientific research documents, whether they are published or not. The documents may come from teaching and research institutions in France or abroad, or from public or private research centers.

Copyright

L'archive ouverte pluridisciplinaire **HAL**, est destinée au dépôt et à la diffusion de documents scientifiques de niveau recherche, publiés ou non, émanant des établissements d'enseignement et de recherche français ou étrangers, des laboratoires publics ou privés.

# JGR Solid Earth

## REPLY

10.1029/2019JB017599

This article is a reply to a comment by Jennings et al. (2019), <https://doi.org/10.1029/2018JB016930>.

### Key Points:

- Secondary X-ray fluorescence from Cu grids impacts metal and silicate measurements equally, nullifying its effect on partition coefficients
- Cu partitioning results from the same diamond anvil cell experiment welded to either a Cu or Mo grid are statistically indistinguishable
- While secondary X-ray fluorescence merits consideration, such effects are wholly inconsequential to the results of Mahan, Siebert, Blanchard, Badro, et al. (2018)

### Supporting Information:

- Supporting Information S1

### Correspondence to:

B. Mahan,  
brandon.mahan@mq.edu.au

### Citation:

Mahan, B., Siebert, J., Badro, J., Borensztajn, S., & Moynier, F. (2019). Reply to comment by Jennings et al. on "Investigating Earth's formation history through copper and sulfur metal-silicate partitioning during core-mantle differentiation". *Journal of Geophysical Research: Solid Earth*, 124, 12,845–12,853. <https://doi.org/10.1029/2019JB017599>

Received 26 FEB 2019

Accepted 17 OCT 2019

Accepted article online 31 OCT 2019

Published online 6 DEC 2019

## Reply to Comment by Jennings et al. on "Investigating Earth's Formation History Through Copper and Sulfur Metal-Silicate Partitioning During Core-Mantle Differentiation"

**B. Mahan<sup>1,2</sup> , J. Siebert<sup>1,3</sup>, J. Badro<sup>1,4</sup> , S. Borensztajn<sup>1</sup>, and F. Moynier<sup>1,3</sup>**

<sup>1</sup>Institut de Physique du Globe de Paris, Université Paris Diderot, Paris, France, <sup>2</sup>Department of Earth and Planetary Sciences, Macquarie University, Sydney, New South Wales, Australia, <sup>3</sup>Institut Universitaire de France, Paris, France, <sup>4</sup>Earth and Planetary Science Laboratory, Ecole Polytechnique Fédérale de Lausanne, Lausanne, Switzerland

**Abstract** Recognizing existing materials that can act as proxies for Earth's building blocks, and understanding the accretionary pathway taken during Earth's growth, persist as outstanding issues in need of resolution. In Mahan, Siebert, Blanchard, Badro, et al. (2018, <https://doi.org/10.1029/2018JB015991>), we conducted diamond anvil cell (DAC) Cu metal-silicate partitioning experiments and coupled these results with a large complement of literature data to characterize Cu metal-silicate partitioning during Earth's core formation and accretion history. The Comment of Jennings, Wade, and Llovet (2019, <https://doi.org/10.1029/2018JB016930>) contends that secondary X-ray fluorescence, originating from the Cu holders that experiments are routinely welded to ("lift-out" grids), compromises the novel Cu partitioning data of Mahan, Siebert, Blanchard, Badro, et al. (2018) beyond utility. To dispel these concerns and further validate our data, we have (i) investigated secondary X-ray fluorescence effects in a Cu-free experiment and provided a matrix-matched data correction, and (ii) rewelded a DAC experiment from a Cu grid to a Mo grid for a comparison of compositional analyses and Cu partitioning results. Secondary fluorescence results, in fact much like the simulated results in Jennings, Wade, and Llovet (2019), indicate that this effect is essentially equal in the metal and silicate phases and therefore has no actual impact on Cu metal-silicate partition coefficients. Moreover, Cu concentrations and partition coefficients determined using the Mo grid are statistically indistinguishable from that determined using the Cu grid. All results decisively illustrate that while secondary X-ray fluorescence must be considered where absolute concentrations are the final objective, it has had no meaningful impact on the partitioning data and observations of Mahan, Siebert, Blanchard, Badro, et al. (2018).

## 1. Introduction

Earth's accretion and core formation is considered the result of the agglomeration of material(s) of various sizes, with large impacts providing enough kinetic energy to melt the majority of the proto-Earth, leading to at least one global deep magma ocean wherein immiscible metal and silicate liquids gravitationally separated at high pressure and temperature, subsequently differentiating the Earth into a core (metal) and mantle (silicate) (Chambers, 2004; Li & Agee, 1996; Tonks & Melosh, 1993; Wetherill, 1989; Wood et al., 2006). With the technical development of the laser-heated diamond anvil cell (DAC) apparatus, experimental metal-silicate partitioning at pressure and temperature conditions that encompass those incurred during terrestrial core-mantle differentiation has defined the frontier of our understanding of element phase partitioning during such processes (e.g., Badro et al., 2015, 2016; Blanchard et al., 2017; Bouhifd & Jephcoat, 2003; Chidester et al., 2017; Fischer et al., 2015; Mahan et al., 2017; Mahan, Siebert, Blanchard, Borensztajn, et al., 2018; Mahan, Siebert, Blanchard, Badro, et al., 2018; Siebert et al., 2012, 2013; Suer et al., 2017). From an analytical standpoint, a key driving force behind the success of such experiments is the use of instrument platforms outfitted with focused ion beam (FIB) instruments for sample recovery and preparation, which make it possible to excavate DAC experiment cross sections (usually ~3 µm thick, 20–30 µm slices) for subsequent elemental abundance quantification either on the same instrument platform, which are often equipped for energy dispersive X-ray spectroscopy (EDX), or at a later point in time by the same or other means (e.g., electron microprobe analysis or EPMA).

The Comment of Jennings, Wade, and Llovet (2019) raises the important point that consideration must be given for the potential effects of secondary X-ray fluorescence, which originates outside the sample and can lead to spurious quantification of *absolute* element concentrations (see also Fournelle et al., 2005; Jennings, Wade, Laurenz, et al., 2019; Wade & Wood, 2012). More pointedly, DAC experiments are routinely welded to Cu transmission electron microscopy (TEM) “lift-out” grids (and Mo to a lesser extent), which provide small prongs ( $\sim 100 \mu\text{m}$ ) to which experimental charges can be welded (often using Pt), but can also be a source of analytical contamination via secondary X-ray fluorescence (namely, continuum or bremsstrahlung X-rays). This is relevant to our previous work (Mahan, Siebert, Blanchard, Badro, et al., 2018), wherein experiment phases (metal and silicate) were analyzed for Cu contents while welded to Cu grids. Being aware of this possible source of contamination, prior to submission of our previous work, we compared EDX and EPMA data, which were found to be in good agreement. Given that these two analytical methods are performed on different instruments, with different geometries and run conditions (e.g., accelerating voltage), this provides first-order evidence that any possible contamination by secondary X-ray fluorescence of the Cu grid did not impart a statistically relevant influence. Jennings, Wade, and Llovet (2019) assert that any difference incurred here due to instrumentation and conditions would have been minor and/or nullified by detector geometry and follow this with detailed Monte Carlo simulations aimed at quantifying secondary X-ray fluorescence from Cu grids for sample geometries that approximate that for *idealized* DAC experiment analyses. From this, Jennings, Wade, and Llovet (2019) report that secondary X-ray fluorescence accounts for approximately 68% and 72% of the signal for metal and silicate phases (respectively), or  $\sim 70\%$  on average. These results are then used to *correct* DAC experimental data from Mahan, Siebert, Blanchard, Badro, et al. (2018) and provide *corrected* Cu partition coefficients,  $\log K_e$ , for three experiments where this correction does not push Cu concentrations in either phase below zero.

In this Reply, we have addressed the Comment of Jennings, Wade, and Llovet (2019) using two complementary approaches to robustly validate the original DAC partitioning data of Mahan, Siebert, Blanchard, Badro, et al. (2018). First, we have assessed secondary X-ray fluorescence by quantifying *apparent* Cu contents (i.e., those generated by secondary fluorescence effects) in the metal and silicate phases of a Cu-free DAC experiment welded to a Cu grid, providing a direct assessment of this effect in (i) a matrix-matched (i.e., like-for-like) experiment and (ii) an analytical geometry that accurately represents those in the analyses of DAC experiments in Mahan, Siebert, Blanchard, Badro, et al. (2018). Moreover, through a significant technical feat in its own right, we have detached a representative DAC experiment of Mahan, Siebert, Blanchard, Badro, et al. (2018) from its original Cu grid and rewelded it onto a Mo grid. Copper concentration measurements and subsequent metal-silicate partition coefficients obtained in both cases are then compared, as the latter case (welded to a Mo grid) is free from potential secondary X-ray fluorescence contamination for Cu quantification.

## 2. Methods

Metal and silicate phases from DAC experiments were analyzed using EDX spectroscopy on the field emission scanning electron microscope (FE-SEM, 15 keV and 5 nA beam current) at the Institut de Physique du Globe de Paris (IPGP), both in the analyses of Mahan, Siebert, Blanchard, Badro, et al. (2018) and in the current work. Recovery of samples was carried out with a FIB instrument coupled to the FE-SEM at IPGP. Prior to sample excavation, a  $\sim 1 \mu\text{m}$  thick strip of Pt was applied to the top of the section for protection from ion bombardment. Thin sections of  $20 \times 30 \times 3 \mu\text{m}$  were then excavated from the center of the hot spot along the compressional axis, characterized by a small metallic spherule ( $d \approx 10 \mu\text{m}$ ) surrounded by quenched glassy matrix (Figure 1 and Figure S1 in Supporting Information). Upon completion of excavation, an *in situ* micromanipulator is used to recover samples from the Re gasket and emplace them on a TEM grid using a Pt weld. With the exception of experiment “PYR K FeS 40” in the present study, all experiments have been attached to a Cu TEM grid. To avoid redundancy and for ease of reading, all other methodological, analytical, and data reduction information can be found in Mahan, Siebert, Blanchard, Badro, et al. (2018). All errors herein are conventionally reported as one standard deviation,  $\sigma$ .

## 3. Results

### 3.1. Quantification of Secondary X-ray Fluorescence From Cu Grids in a DAC Experiment

In order to assess the contribution of secondary X-ray fluorescence to the overall signal for typical DAC experiments welded to Cu grids, and to determine the spatial distribution of this effect, a linear transect of

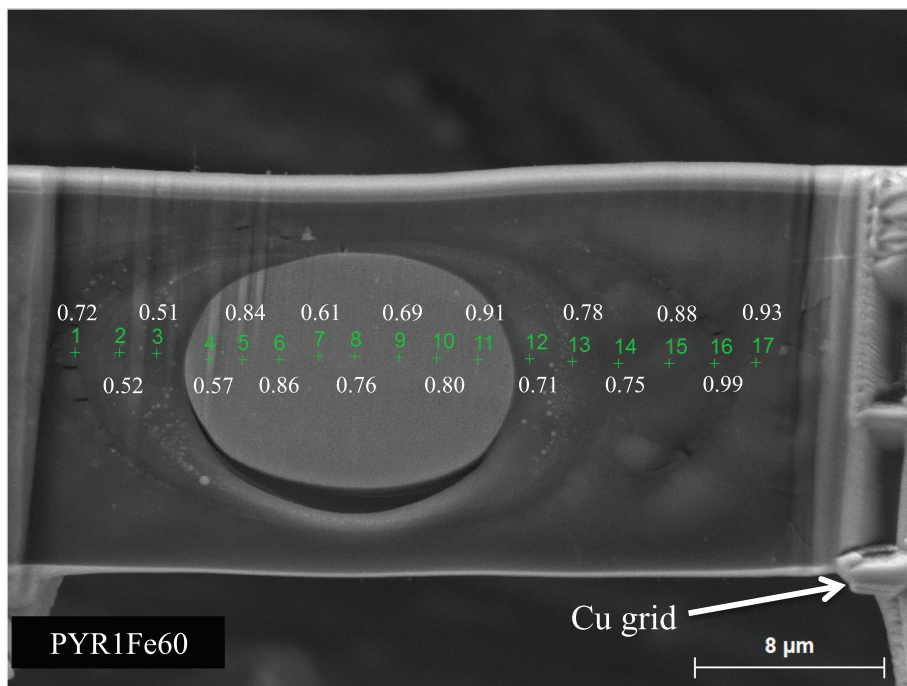


**Figure 1.** Backscatter electron (BSE) image of “PYR1Fe60” (71 GPa and 4,000 K; from Badro et al., 2018), a Cu-free experiment used in this study to assess secondary fluorescence from the Cu TEM grid. The metallic phase is represented by the large spherule at the center of the experimental charge (light grey), which is surrounded by quenched silicate glass (dark grey), with small stranded metallic globules (bright spots) dispersed within the silicate fraction. The lighter color of the silicate surrounding the metal is due to increased FeO content relative to the starting material (the unreacted silicate encasing the experiment). Green crosses and numbers represent point analyses, and values in white indicate Cu and Cu oxide abundances (in wt. %) for the metal and silicate phases, respectively.

point analyses was conducted across a Cu-free experiment (“PYR1Fe60” from Badro et al., 2018) (Figure 1). In Figure 1, “PYR1Fe60” is welded to a Cu grid at the right, and *apparent* Cu concentrations, i.e., those produced as a result of secondary X-ray fluorescence, are indicated above or below each analytical point. The average *apparent* Cu concentration for the metallic phase is  $0.76 \text{ wt.\%} \pm 0.12$  and  $0.76 \pm 0.17$  oxide wt. % in the silicate phase. These values were then subtracted from EDX Cu concentration data for DAC experiment “BAS K Fe 60” (this experiment is also in Mahan, Siebert, Blanchard, Badro, et al., 2018) (Table 1), revealing a 46% contribution to the EDX signal for the metallic phase and 52% for the silicate phase, or approximately 50% in either case, and providing *corrected* Cu concentrations for “BAS K Fe 60” (Table 1). Subsequently, the Cu metal-silicate partition coefficient for “BAS K Fe 60” was recalculated using these *corrected* values, yielding a *corrected*  $\log K_e$  of  $0.45 \pm 0.24$  (up from  $0.29 \pm 0.07$  in Mahan, Siebert, Blanchard, Badro, et al., 2018) (Figure 2; Table 2). Table 1 reports all relevant EDX compositional data. Table 2 reports all experiments and conditions relevant to the current work, along with all relevant  $\log K_e$  values from Mahan, Siebert, Blanchard, Badro, et al. (2018), Jennings, Wade, and Llovet (2019), and this work. Within error, all  $\log K_e$  values agree.

### 3.2. Quantification of Cu in a DAC Experiment Welded to a Mo Grid Versus a Cu grid

To quantify Cu concentrations in an environment with no potential for secondary fluorescence contamination, the DAC experiment “PYR K FeS 40” from Mahan, Siebert, Blanchard, Badro, et al. (2018) was carefully removed from its original Cu grid and rewelded to a Mo grid, and its metal and silicate composition was reanalyzed via EDX (Figure S1, Table 1). Compositional data for this experiment welded both to the Mo grid and Cu grid are compared side-by-side in Table 1—all concentrations measurements are in agreement, notably including Cu. The  $\log K_e$  value determined from Mo grid analysis ( $0.56 \pm 0.08$ ), the original value reported in Mahan, Siebert, Blanchard, Badro, et al. (2018) ( $0.54 \pm 0.07$ ; Cu grid, EPMA analysis), the value calculated

**Table 1**  
Average Composition of Quenched Metal (wt. %) and Silicate (Oxide wt. %) Melts by EDX

| Experiment                     | BAS K Fe 60 (Cu grid, EDX) | $\sigma$ | PYR1Fe60 (Cu grid, EDX) | $\sigma$ | BAS K Fe 60 (corrected) | $\sigma$          | PYR K FeS 40 (Cu grid, EDX) | $\sigma$ | PYR K FeS 40 (Mo grid, EDX) | $\sigma$ |      |
|--------------------------------|----------------------------|----------|-------------------------|----------|-------------------------|-------------------|-----------------------------|----------|-----------------------------|----------|------|
| Metal (wt%)                    | $N = 2$                    |          | $N = 8$                 |          | $N = 2$                 |                   | $N = 5$                     |          | $N = 13$                    |          |      |
| O                              | 10.17                      | 0.38     |                         |          | 10.17                   | 0.38              | 7.41                        | 0.33     | 8.21                        | 1.09     |      |
| Mg                             | ---                        | ---      |                         |          | ---                     | ---               | ---                         | ---      | ---                         | ---      |      |
| Al                             | ---                        | ---      |                         |          | ---                     | ---               | ---                         | ---      | ---                         | ---      |      |
| Si                             | 1.35                       | 0.28     |                         |          | 1.35                    | 0.28              | 1.68                        | 0.23     | 1.80                        | 0.46     |      |
| P                              |                            |          |                         |          |                         |                   | 5.20                        | 0.04     | 5.09                        | 0.32     |      |
| S                              |                            |          |                         |          |                         |                   |                             |          |                             |          |      |
| K                              | ---                        | ---      |                         |          | ---                     | ---               | ---                         | ---      | ---                         | ---      |      |
| Fe                             | 75.4                       | 0.7      |                         |          | 75.4                    | 0.7               | 76.97                       | 0.71     | 75.91                       | 1.29     |      |
| Cu                             | 1.66                       | 0.05     | 0.76                    |          | 0.12                    | 0.90 <sup>a</sup> | 0.13                        | 6.22     | 0.07                        | 6.19     | 0.40 |
| Zn                             | ---                        | ---      |                         |          | ---                     | ---               | ---                         | ---      | ---                         | ---      |      |
| Pb                             | ---                        | ---      |                         |          | ---                     | ---               | ---                         | ---      | ---                         | ---      |      |
| U                              | ---                        | ---      |                         |          | ---                     | ---               | ---                         | ---      | ---                         | ---      |      |
| Total                          | 99.81                      |          | N/A                     |          | 99.05                   |                   |                             |          | 99.84                       |          |      |
| Silicate (oxide wt%)           | $N = 7$                    |          | $N = 9$                 |          | $N = 7$                 |                   | $N = 8$                     |          | $N = 11$                    |          |      |
| Na <sub>2</sub> O              |                            |          |                         |          |                         |                   |                             |          |                             |          |      |
| MgO                            | 6.83                       | 0.15     |                         |          | 6.83                    | 0.15              | 21.31                       | 1.38     | 17.89                       | 1.05     |      |
| K <sub>2</sub> O               |                            |          |                         |          |                         |                   |                             |          |                             |          |      |
| Al <sub>2</sub> O <sub>3</sub> | 11.39                      | 0.29     |                         |          | 11.39                   | 0.29              | 3.42                        | 0.27     | 2.86                        | 0.24     |      |
| CaO                            | 2.02                       | 0.06     |                         |          | 2.02                    | 0.06              | 2.89                        | 0.18     | 3.35                        | 0.12     |      |
| SiO <sub>2</sub>               | 32.77                      | 0.77     |                         |          | 32.77                   | 0.77              | 33.28                       | 1.80     | 31.23                       | 1.20     |      |
| SO <sub>2</sub>                |                            |          |                         |          |                         |                   | 0.56                        | 0.12     |                             |          |      |
| FeO                            | 32.82                      | 0.92     |                         |          | 32.82                   | 0.92              | 27.51                       | 3.56     | 31.81                       | 2.11     |      |
| CuO                            | 1.45                       | 0.32     | 0.76                    |          | 0.17                    | 0.70 <sup>a</sup> | 0.36                        | 2.94     | 0.38                        | 2.59     | 0.28 |
| TiO <sub>2</sub>               |                            |          |                         |          |                         |                   |                             |          |                             |          |      |
| ZnO                            |                            |          |                         |          |                         |                   |                             |          |                             |          |      |
| Total                          | 102.98                     |          | N/A                     |          | 102.22                  |                   |                             |          | 98.49                       |          |      |

<sup>a</sup>Abundances determined by subtracting average *apparent* Cu concentrations caused by secondary X-ray fluorescence from Cu grids in sample PYR1Fe60.

herein ( $0.50 \pm 0.10$ ), and the *corrected* value estimated from Jennings, Wade, and Llovet (2019) (0.56) are all statistically indistinguishable (Table 2).

## 4. Discussion

### 4.1. Secondary X-ray Fluorescence in DAC Experiment Analyses and Comparison to Jennings, Wade, and Llovet (2019)

The linear transect detailed in Figure 1 provides a direct account of secondary X-ray fluorescence effects derived from Cu grids in a typical DAC metal-silicate experiment such as those analyzed in Mahan, Siebert, Blanchard, Badro, et al. (2018). It is readily apparent that the Cu grid does indeed impart a measurable effect on the overall EDX signal, accounting for approximately 50% in both metal and silicate phases. Although *apparent* Cu concentrations directly adjacent to the Cu grid approach a statistically significant enrichment relative to those farthest away, these point analyses are in the unreacted (i.e., unmelted) portion of the silicate phase and therefore are well outside the zone of compositional analyses for DAC experiments (i.e., unreacted silicate is avoided). With this in mind, it is demonstrable from Figure 1 that—as opposed to the simulated results of Jennings, Wade, and Llovet (2019)—the spatial distribution of secondary X-ray fluorescence in the *live* scenario is essentially a wash. That is to say that given typical errors associated with EDX (and EPMA) measurements on the order of 0.1–1.0 wt. %, and an overall spread in *apparent* Cu concentrations of ~0.3 wt. % along the transect of “PYR1Fe60” (not including points 15–17 in the unreacted zone), the effect of secondary X-ray fluorescence from the Cu grid is evenly distributed (homogeneous) throughout the experimental charge. Thus, although secondary fluorescence from Cu grids would certainly be a concern

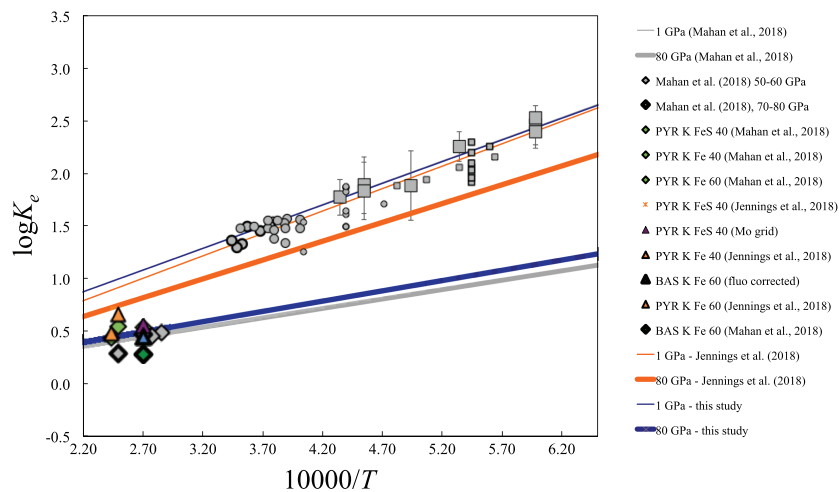


**Figure 2.** Exchange coefficients,  $\log K_e$ , plotted as a function of reciprocal temperature ( $10,000/T$ ). Diamond anvil cell experiments from Mahan, Siebert, Blanchard, Badro, et al. (2018) are indicated by diamonds: grey diamonds indicate experiments that have not been addressed herein, and green diamonds indicate experiments that have been addressed either by Jennings, Wade, and Llovet (2019) or the current work. *Corrected*  $\log K_e$  values from Jennings, Wade, and Llovet (2019) are indicated by orange triangles (estimated from Figure 6 of their work). The blue triangle represents “BAS K Fe 60” as *corrected* in the current study, and the purple triangle represents the  $\log K_e$  of “PYR K FeS 40” as determined when welded to a Mo grid. Note that for “PYR K FeS 40”, the original value from Mahan, Siebert, Blanchard, Badro, et al. (2018), *corrected* value from Jennings, Wade, and Llovet (2019), and the value as determined on an Mo grid all overlap in the Figure 1. 1 and 80 GPa regression model isobars from Mahan, Siebert, Blanchard, Badro, et al. (2018) are indicated by thin and thick grey lines, respectively; 1 and 80 GPa regression model isobars generated using *corrected* data from Jennings, Wade, and Llovet (2019) are indicated by thin and thick orange lines, respectively; 1 and 80 GPa regression model isobars from the current study are indicated by thin and thick blue lines, respectively.

for quantifying trace *absolute* Cu abundances, for example in small independent melt or mineral phases in a heterogeneous matrix, within the current context where what is being calculated is the *relative* distribution of Cu between two major constituent phases, secondary fluorescence effects can be effectively subtracted out. This has been done for the experiment “BAS K Fe 60” from Mahan, Siebert, Blanchard, Badro, et al. (2018) (an experiment deemed irretrievable in Jennings, Wade, and Llovet, 2019) generating a  $\log K_e$  value for this experiment that is less than 0.2 higher than that reported in Mahan, Siebert, Blanchard, Badro, et al. (2018) (Figure 2). This difference is on par with or less than typical errors and variability associated with metal-silicate partition coefficients regardless of apparatus or analytical technique (e.g. literature data in Figure 2 of Mahan, Siebert, Blanchard, Borensztajn, et al., 2018; Mahan, Siebert, Blanchard, Badro, et al., 2018) and renders the original and *corrected* partition coefficients for this experiment the same within error, an observation that extends to all data within Mahan, Siebert, Blanchard, Badro, et al.

**Table 2**  
*P, T, and  $\log K_e$  Values for All Relevant Experiments*

| Experiment   | Source  | P (GPa) | T (K) | $\log K_e$        | $\sigma$ |
|--------------|---|---------|-------|-------------------|----------|
| BAS K Fe 60  | Mahan, Siebert, Blanchard, Badro, et al. (2018) | 70      | 3,700 | 0.28 <sup>a</sup> | 0.07     |
|              | This study ( <i>corrected</i> )                 |         |       | 0.45 <sup>b</sup> | 0.24     |
| PYR K FeS 40 | Mahan, Siebert, Blanchard, Badro, et al. (2018) | 49      | 3,700 | 0.54 <sup>a</sup> | 0.07     |
|              | Jennings, Wade, and Llovet (2019)               |         |       | 0.56 <sup>c</sup> | ---      |
|              | This study ( <i>Cu grid</i> )                   |         |       | 0.50 <sup>b</sup> | 0.10     |
| PYR K Fe 40  | This study ( <i>Mo grid</i> )                   |         |       | 0.56 <sup>b</sup> | 0.08     |
|              | Mahan, Siebert, Blanchard, Badro, et al. (2018) | 54      | 4,000 | 0.55 <sup>a</sup> | 0.17     |
|              | Jennings, Wade, and Llovet (2019)               |         |       | 0.66 <sup>c</sup> | ---      |
| PYR K Fe 60  | Mahan, Siebert, Blanchard, Badro, et al. (2018) | 71      | 4,100 | 0.44 <sup>a</sup> | 0.11     |
|              | Jennings, Wade, and Llovet (2019)               |         |       | 0.48 <sup>c</sup> | ---      |

<sup>a</sup> $\log K_e$  values calculated from EPMA data in original study. <sup>b</sup> $\log K_e$  values calculated from EDX data in this work. <sup>c</sup> $\log K_e$  values estimated from Figure 6 in Jennings, Wade, and Llovet (2019).

(2018). Put more explicitly, these results demonstrate that contrary to the assertion made in Jennings, Wade, and Llovet (2019), the data set of Mahan, Siebert, Blanchard, Badro, et al. (2018) is not only *correctable*, but is essentially uncompromised by secondary X-ray fluorescence based on these observations alone, and therefore no correction is needed and the data stand as they are.

The resultant contribution of secondary X-ray fluorescence from Cu grids as outlined in Jennings et al. (2019), ~70% for both metal and silicate phases, is substantially larger than that observed in the current work, at ~50% in both phases. Although a detailed exploration into where this ~20% difference arises is far outside the scope of the current work, it is likely the cumulative result of multiple contributing factors, such as:

1. The approach taken by Jennings, Wade, and Llovet (2019) to investigate the potential effects of secondary X-ray fluorescence from Cu grids, which is largely based on Monte Carlo simulations in which idealized compositions are used (pure Fe for metal, CFMAS for silicate), and therefore does not fully encapsulate the experimental compositions of Mahan, Siebert, Blanchard, Badro, et al. (2018).
2. The sample lamella simulated, at  $20 \times 12 \times 3 \mu\text{m}$ , are less than half the size of those typically found in Mahan, Siebert, Blanchard, Badro, et al. (2018) (approximately  $20 \times 30 \times 3 \mu\text{m}$ ), which may focus and/or enhance the effects of secondary X-ray fluorescence.
3. The simulations of Jennings, Wade, and Llovet (2019) differ from typical DAC experimental run products as they assume that all silicate has melted to become basaltic glass, which is not the case (see Figures 1 and S1; Mahan, Siebert, Blanchard, Borensztajn, et al., 2018; Mahan, Siebert, Blanchard, Badro, et al., 2018), and thus these simulations also cannot account for the size, structure, and/or geometry of this reaction zone.
4. The simulations of Jennings, Wade, and Llovet (2019) furthermore do not account for the Pt welding, gaps between the metal and silicate phases (from differential thermal expansion/contraction), surface topography, TEM grid orientation relative to samples, or any other morphological features and variables that are typical of actual DAC experiments.

In summary, regardless of the cause(s) of the heightened secondary X-ray fluorescence observed in the simulations of Jennings, Wade, and Llovet (2019) relative to that observed herein, the most salient points are (i) that in both cases and within error, secondary fluorescence affects both phases equally; (ii) that in the live-action case of this work (not simulated), *apparent* Cu concentrations do not vary considerably along a transect that should detect the maximum difference possible (i.e., a line perpendicular to the Cu grid); and (iii) that in any case, so-called *corrected* values are statistically indistinguishable from the original  $\log K_e$  values reported in Mahan, Siebert, Blanchard, Badro, et al. (2018). All of these points bolster the validity of the original data of Mahan, Siebert, Blanchard, Badro, et al. (2018), as although minor differences are detectable, they are inconsequential.

#### 4.2. Copper Partitioning Results From “PYR K FeS 40” Welded to a Cu Grid Versus Mo Grid

Applying a correction to account for secondary fluorescence inherently brings with it higher propagated errors and may leave factions of the community unconvinced. Therefore, a representative experiment from Mahan, Siebert, Blanchard, Badro, et al. (2018), “PYR K FeS 40” (Figure 1 in our previous work), which has been analyzed via EDX, was carefully detached from its Cu grid and rewelded to a Mo grid, where it was again been analyzed via EDX for a more direct account of any potential effects of secondary X-ray fluorescence on Cu concentration measurements and subsequent calculated partition coefficients. The compositional data for “PYR K FeS 40” are in very good agreement between both grids (Table 1, Figure 2). Furthermore, the calculated  $\log K_e$  from the Mo grid, that reported in Mahan, Siebert, Blanchard, Badro, et al. (2018), and the estimated *corrected* value from Jennings, Wade, and Llovet (2019) are all the same within error (Table 2). The only notable difference being that any *corrected* values carry with them larger analytical uncertainties due to the larger number of mathematical operations involved. However, even the larger errors associated with *corrected* values (Jennings, Wade, and Llovet (2019) and this work) are not significantly different from (or larger than) those typical of  $\log K_e$  calculations in the literature. The results of “PYR K FeS 40” attached to the Mo grid versus the Cu grid robustly illustrate that while there is undoubtedly secondary X-ray fluorescence from Cu grids that can influence absolute concentration measurements, this has not altered or compromised the data or interpretations of Mahan, Siebert, Blanchard, Badro, et al. (2018) in any significant or noteworthy way.

**Table 3**  
*Multiple Linear Regression Coefficients*

| Source   | n  | a                         | b             | c        |
|--|----|---------------------------|---------------|----------|
| Mahan, Siebert, Blanchard, Badro, et al. (2018)  | 60 | -0.03 (0.15) <sup>a</sup> | 0.415 (0.030) | -29 (6)  |
| Corgne et al. (2008)                             | 14 | 0.3                       | 0.23          | -37 (45) |
| Vogel (2015) <sup>b</sup>                        | 17 | 0.94 (0.37)               | 0.187 (0.088) | -30 (12) |
| Jennings, Wade, and Llovet (2019) <i>Comment</i> | 55 | -0.1 (0.1)                | 0.425 (0.026) | -9 (7)   |
| This study                                       | 60 | -0.03 (0.15)              | 0.413 (0.029) | -27 (6)  |

<sup>a</sup>Values in parenthesis indicated error as one standard deviation ( $\sigma$ ). <sup>b</sup>Regression constants determined using original data from Vogel (2015).

#### 4.3. Impact on Cu Metal-Silicate Partitioning Characterization

Table 3 reports (above the partition) multiple linear regression results, that is, the regression constants that characterize the metal-silicate partitioning of Cu as a function of temperature ( $b$  constant) and pressure ( $c$  constant), as reported in our previous work (Mahan, Siebert, Blanchard, Badro, et al., 2018), along with those reported in Corgne et al. (2008) and those generated from the data of Vogel (2015), for reference. Below the partition of Table 3, we report calculated regression constants using the *corrected* values given by the Comment of Jennings, Wade, and Llovet (2019) and calculated regression constants using all *corrected* data (Jennings, Wade, & Llovet 2019 and this work) along with results from analysis on the Mo grid. To project an accurate depiction of any potential influence(s) of data correction, and because the present study further validates the DAC data of Mahan, Siebert, Blanchard, Badro, et al. (2018), the final regression constants of the current work were calculated including all original data from Mahan, Siebert, Blanchard, Badro, et al. (2018) that have not been addressed herein, along with those that have. First, the regression constants for already published work (above partition) demonstrate that Mahan, Siebert, Blanchard, Badro, et al. (2018) is not the only study to have indicated a marginal pressure effect on Cu metal-silicate partitioning, and simply is the first to have produced a pressure effect with an associated error that is less than the value of the constant itself, that is, one that is statistically significant (Table 3 and references therein). This has less to do with any pressure effect itself and more to do with the fact that Mahan, Siebert, Blanchard, Badro, et al. (2018) provided high pressure and temperature data from DAC experiments to bring higher resolution to this constant. Second, it is worth noting that the Cu metal-silicate partitioning parameterization of Mahan, Siebert, Blanchard, Badro, et al. (2018) is calculated from a much larger dataset than any previous study, with  $\sim 4 \times$  more data points ( $n$  in Table 3), and synthesizes data across numerous studies from experiments in multiple apparatus types, thereby providing the most comprehensive and broadly consistent view of Cu metal-silicate partitioning currently available. Lastly, when compared to the original characterization of Mahan, Siebert, Blanchard, Badro, et al. (2018), the regression constants generated in this study—using original and *corrected* data and data from the Mo grid—are statistically indistinguishable to those originally reported in Mahan, Siebert, Blanchard, Badro, et al. (2018) (Table 3). This clearly demonstrates that any data corrections and even re-analysis on a Cu-free (Mo) grid do not change the results in any meaningful way.

To illustrate this another way, in Figure 2, we have included 1 and 80 GPa model isobars generated using the regression constants from (i) Mahan, Siebert, Blanchard, Badro, et al. (2018), (ii) *corrected* data from Jennings, Wade, and Llovet (2019), and (iii) original, corrected, and reanalyzed data from the current study. The 1 GPa isobars of all models overlap. The 80 GPa isobar generated using data from Jennings, Wade, and Llovet (2019) does indeed show a smaller (though still existent) pressure effect. However this is largely due to the fact that only three of eight DAC experiments have been included in this regression. The 80 GPa isobars from Mahan, Siebert, Blanchard, Badro, et al. (2018) and the current work are essentially the same, graphically illustrating the inconsequential effect of any data *corrections* or re-analyses on Cu-free grids and validating the original modeling, as both isobars intersect the high pressure data while also accurately characterizing all lower pressure data, again evidencing a stalwart model given the spread in experimental labs, conditions, and apparatuses included. Finally, all regression models trend toward convergence as temperature increases, and when considering plausible final temperatures for core formation in Earth, at greater than  $\sim 3,500$  K ( $10,000/T < \sim 2.8$ ) (e.g., Badro et al., 2015; Siebert et al., 2012, 2013), the differences between all these regression models diminish even further (Figure 2). Taking all of the above points together, it is readily discernible that while it is possible to *correct* the original data of Mahan, Siebert, Blanchard, Badro, et al.

(2018), such corrections are of very limited utility in this context, have no consequential impact on the thermodynamic characterization of Cu metal-silicate partitioning, and do not impact any subsequent modeling or observations built off of this parameterization.

## 5. Conclusions

We have clearly, concisely and decisively demonstrated that the Cu metal-silicate partitioning data in our previous work, Mahan, Siebert, Blanchard, Badro, et al. (2018), have not been compromised by secondary X-ray fluorescence from their Cu TEM grid hosts in any meaningful way. This has been accomplished by detailing secondary X-ray fluorescence from Cu grids in an actual/typical DAC metal-silicate experiment and by making a side-by-side comparison of compositional results from the same DAC experiment welded to either a Cu or Mo grid. Both approaches robustly validate the original data of Mahan, Siebert, Blanchard, Badro, et al. (2018). Original and *corrected* Cu partition coefficients,  $\log K_e$ , from Jennings, Wade, and Llovet (2019) and the current study are all the same within error, and moreover,  $\log K_e$  values for the same experiment attached to either a Cu or Mo grid are statistically indistinguishable. In summary, while it is true that secondary X-ray fluorescence contamination can be significant and deleterious in other contexts, due to (i) its largely homogeneous distribution across a typical DAC metal-silicate experiment and (ii) the fact that partition coefficients are *relative* values and not *absolute* concentrations, secondary X-ray fluorescence from Cu grids has in no way compromised the results, modeling, or interpretations of Mahan, Siebert, Blanchard, Badro, et al. (2018). In summation, our previous work stands on its own and is resoundingly validated by the present study.

## Acknowledgments

We very warmly thank Mike Crowner, Erin Syring, and Stephen Parman at *JGR: Solid Earth* for their handling of this Comment/Reply cycle. We acknowledge the financial support of the UnivEarthS Labex program at Sorbonne Paris Cité (ANR-10-LABX-0023 and ANR-11-IDEX-0005-02). FIB and SEM instruments are supported by the IPGP multidisciplinary program PARI and by Paris-IdF region SESAME Grant 12015908. BM thanks the financial support of the IDEX SPC through a PhD fellowship. JS thanks the financial support of the French National Research Agency (ANR) Project VolTerre, Grant ANR-14-CE33-0017-01. JB acknowledges funding from the European Research Council under the European Community's Seventh Framework Programme (FP7/2007–2013)/ERC Grant agreement 207467 (DECORE). FM acknowledges funding from the European Research Council under the H2020 framework program/ERC Grant agreement 637503 (Pristine), and the ANR through a *chaire d'excellence* Sorbonne Paris Cité. All original data used in calculating Cu metal-silicate equilibrium constants can be found in this paper; historical data and modeling equations can be found in Mahan, Siebert, Blanchard, Badro, et al. (2018) and Suer et al. (2017), respectively.

## References

- Badro, J., Aubert, J., Hirose, K., Nomura, R., Blanchard, I., Borensztajn, S., & Siebert, J. (2018). Magnesium partitioning between Earth's mantle and core and its potential to drive an early exsolution geodynamo. *Geophysical Research Letters*, 45(24), 13,240–13,248.
- Badro, J., Brodholt, J. P., Piet, H., Siebert, J., & Ryerson, F. J. (2015). Core formation and core composition from coupled geochemical and geophysical constraints. *Proceedings of the National Academy of Science*, 112, 12,310–12,314.
- Badro, J., Siebert, J., & Nimmo, F. (2016). An early geodynamo driven by exsolution of mantle components from the Earth's core. *Nature*, 536(7616), 326–328. <https://doi.org/10.1038/nature18594>
- Blanchard, I., Siebert, J., Borensztajn, S., & Badro, J. (2017). The solubility of heat-producing elements in Earth's core. *Geochemical Perspect. Lett.*, 5, 1–5.
- Bouhifd, M. A., & Jephcoat, A. P. (2003). The effect of pressure on partitioning of Ni and Co between silicate and iron-rich metal liquids: a diamond-anvil cell study. *Earth and Planetary Science Letters*, 209(1–2), 245–255.
- Chambers, J. E. (2004). Planetary accretion in the inner solar system. *Earth and Planetary Science Letters*, 223, 241–252.
- Chidester, B. A., Rahman, Z., Righter, K., & Campbell, A. J. (2017). Metal-silicate partitioning of U: Implications for the heat budget of the core and evidence for reduced U in the mantle. *Geochimica et Cosmochimica Acta*, 199, 1–12.
- Corgne, A., Keshav, S., Wood, B. J., McDonough, W. F., & Fei, Y. (2008). Metal-silicate partitioning and constraints on core composition and oxygen fugacity during Earth accretion. *Geochimica et Cosmochimica Acta*, 72, 574–589.
- Fischer, R. A., Nakajima, Y., Campbell, A. J., Frost, D. J., Harries, D., Langenhorst, F., & Rubie, D. C. (2015). High pressure metal-silicate partitioning of Ni, Co, V, Cr, Si, and O. *Geochimica et Cosmochimica Acta*, 167, 177–194.
- Fournelle, J. H., Kim, S., & Perepezko, J. H. (2005). Monte Carlo simulation of Ni<sup>2+</sup> secondary fluorescence in EPMA: Comparison of PENELOPE simulations with experimental results. *Surface and Interface Analysis: An International Journal devoted to the development and application of techniques for the analysis of surfaces, interfaces and thin films*, 37(11), 1012–1016. <https://doi.org/10.1002/sia.2114>
- Jennings, E. S., Wade, J., & Llovet, X. (2019). Comment on “Investigating Earth's formation history through copper & sulfur metal-silicate partitioning during Core-mantle differentiation” by Mahan et al., *Journal of Geophysical Research: Solid Earth*, 124. <https://doi.org/10.1029/2018JB016930>
- Jennings, E. S., Wade, J., Laurenz, V., & Petitgirard, S. (2019). Diamond anvil cell partitioning experiments for accretion and core formation: Testing the limitations of electron microprobe analysis. *Microscopy and Microanalysis*, 25(1), 1–10. <https://doi.org/10.1017/S1431927618015568>
- Li, J., & Agee, C. B. (1996). Geochemistry of mantle-core differentiation at high pressure. *Nature*, 381(6584), 686–689. <https://doi.org/10.1038/381686a0>
- Mahan, B., Siebert, J., Blanchard, I., Badro, J., Kubik, E., Sossi, P., & Moynier, F. (2018). Investigating Earth's formation history through copper & sulfur metal-silicate partitioning during core-mantle differentiation. *Journal of Geophysical Research: Solid Earth*, 123, 8349–8363. <https://doi.org/10.1029/2018JB015991>
- Mahan, B., Siebert, J., Blanchard, I., Borensztajn, S., Badro, J., & Moynier, F. (2018). Constraining compositional proxies for Earth's accretion and core formation through high pressure and high temperature Zn and S metal-silicate partitioning. *Geochimica et Cosmochimica Acta*, 235, 21–40. <https://doi.org/10.1016/j.gca.2018.04.032>
- Mahan, B. M., Siebert, J., Pringle, E. A., & Moynier, F. (2017). Elemental partitioning and isotopic fractionation of Zn between metal and silicate and geochemical estimation of the S content of the Earth's core. *Geochimica et Cosmochimica Acta*, 196, 252–270. <https://doi.org/10.1016/j.gca.2016.09.013>
- Siebert, J., Badro, J., Antonangeli, D., & Ryerson, F. J. (2012). Metal-silicate partitioning of Ni and Co in a deep magma ocean. *Earth and Planetary Science Letters*, 321–322, 189–197. <https://doi.org/10.1016/j.epsl.2012.01.013>
- Siebert, J., Badro, J., Antonangeli, D., & Ryerson, F. J. (2013). Terrestrial accretion under oxidizing conditions. *Science*, 339(6124), 1194–1197. <https://doi.org/10.1126/science.1227923>

- Suer, T.-A., Siebert, J., Remusat, L., Menguy, N., & Fiquet, G. (2017). A sulfur-poor terrestrial core inferred from metal-silicate partitioning experiments. *Earth and Planetary Science Letters*, 469, 84–97. <https://doi.org/10.1016/j.epsl.2017.04.016>
- Tonks, W. B., & Melosh, H. J. A. Y. (1993). Magma ocean formation due to giant impacts. *Journal of Geophysical Research*, 98(E3), 5319–5333. <https://doi.org/10.1029/92JE02726>
- Vogel, A. K. (2015). *Siderophile element partitioning at high pressure and temperatures - implications for core formation processes*. PhD thesis. Germany: Universität Bayreuth.
- Wade, J., & Wood, B. J. (2012). Metal-silicate partitioning experiments in the diamond anvil cell: A comment on potential analytical errors. *Physics of the Earth and Planetary Interiors*, 192–193, 54–58. <https://doi.org/10.1016/j.pepi.2011.12.002>
- Wetherill, G. W. (1989). The formation of the Solar System: Consensus, alternatives, and missing factors. In H. A. Weaver & L. Danly (Eds.), *The formation and evolution of planetary systems* (pp. 1–30). Cambridge: Cambridge University Press.
- Wood, B. J., Walter, M. J., & Wade, J. (2006). Accretion of the Earth and segregation of its core. *Nature*, 441(7095), 825–833. <https://doi.org/10.1038/nature04763>